TECHNICAL ARTICLE



Failure Mode Analysis of Microstructural Alignment in Freeze-Cast Scaffolds Using FEM

Maddie A. Schmitz¹ · Jacob Hochhalter¹ · Steven E. Naleway¹

Received: 7 February 2025 / Accepted: 14 April 2025 © The Minerals, Metals & Materials Society 2025

Abstract

Magnetic freeze-casting is a promising technique to create structures that are lightweight, yet relatively high strength for applications in aerospace, biomedical devices, and bone and tissue implants. Freeze-cast scaffolds previously have been hampered by a lack of strength in directions orthogonal to freezing, but recent work using fields generated by Helmholtz coils has provided a unique solution to effectively fully align the microstructure and increase ultimate compressive strength (UCS). Though the increase in strength that comes with aligning the microstructure is well documented, little is known about how this changes the failure mode of the scaffold. This work uses finite element models created from micro computed tomography (CT) scans of freeze-cast scaffolds, which are validated using experimental results. These models provide insight into the dominant failure mode of freeze-cast scaffolds and how it changes with microstructural alignment. The energy absorbed by different failure modes (e.g., buckling, ultimate compressive failure) within the magnetically freeze-cast scaffolds enables more informed applications and tailored scaffolds to best suit their applications.

Introduction

Materials that are lightweight, yet relatively high strength present a unique combination of properties that are of interest for a number of applications. Developing additional lightweight high-strength materials could advance technologies in the biomedical and aerospace fields. Within the biomedical field, this combination of properties and the porous nature of freeze-cast scaffolds makes them a prime candidate for bone and tissue implants [1, 2]. In the aerospace industry, freeze-cast scaffolds could be employed as light weight structural components (e.g., brackets, frames, internal supports) and thermal protection systems (e.g., heat shields, engine components exposed to high temperatures) [1–3]. Porous structures, especially those found in nature, have been known to be particularly effective in creating this high strength at low weights. One way is to create a porous structure through freeze-casting [2–6]. The freeze-casting process consists of four steps. First, a slurry is prepared by combing some solid loading, binders, dispersant, and liquid freezing agent (e.g. water) and homogenized through

Much work has been done in the field to increase microstructural strength in these directions perpendicular to ice growth. One way to create microstructural alignment in freeze-cast scaffolds is through the use of energized fields [7, 8, 11]. In the absence of any energized field, the lamellar walls in the directions orthogonal to freeze-casting are randomly oriented in all directions [12, 13]. When an external field is applied, a directionality of these walls can be induced, which is referred to as microstructure alignment. Previous work has shown that microstructural alignment increases ultimate compressive strength (UCS) in that direction [7, 14–16]. Using energized fields (e.g., electric

Published online: 04 June 2025



mixing. Second, the slurry is directionally frozen at a distinct rate to facilitate ice growth in dendritic form and create a solid sample. Third, ice crystals are removed by sublimating the sample. A porous structure, referred to as a green scaffold, where the remaining material forms a negative of the ice crystals is left after this step. Lastly, green scaffolds are sintered at high temperatures to solidify the structure, resulting in a solid porous structure referred to as a freeze-cast scaffold. One major limitation of freeze-cast scaffolds to date is that in the direction of freezing freeze-cast scaffolds have high compressive strength, but in the directions orthogonal to freezing strength is greatly lacking. This lack of compressive strength results from an absence of microstructure alignment [7–10].

Maddie A. Schmitz maddie.schmitz@utah.edu

Department of Mechanical Engineering, University of Utah, Salt Lake City, USA

fields, magnetic fields, and ultrasonic waves) can create this microstructural alignment to increase UCS in directions lacking strength while maintaining the strength in the direction of ice growth [9, 12, 15, 17, 18]. Magnetic fields have been known to be especially effective in increasing the microstructural alignment, which has resulted in drastic improvements in mechanical properties, with specific reports detailing an increase of 200% in both the Young's modulus and strength of scaffolds [3, 7, 14–16]. Extensive work has been done to achieve microstructural alignment through employing permanent magnets [7, 8, 16, 17]. Though they are high in strength, fields generated by permanent magnets are low in uniformity, which causes particle agglomeration in the scaffold [15, 18, 19]. These particle agglomerations result in nonuniform microstructure alignment and stress concentrations, which decrease the strength of the scaffold [20]. Helmholtz coils are known to generate highly uniform magnetic fields and thus have been revolutionary in creating highly aligned freeze-cast scaffolds free of agglomeration and stress concentrations [14, 21, 22].

Helmholtz coils have been effective at creating microstructural alignment in freeze-cast scaffolds with iron oxide due to its ferromagnetic nature. In recent work, effectively 100% microstructural alignment was achieved in iron oxide scaffolds using magnetic fields generated by Helmholtz coils [23]. Prior to this work, complete microstructural control using Helmholtz coils was not possible. Of additional impact is that the aligned microstructure is uniform throughout and free of particle agglomerations, thanks to the highly uniform nature of fields created by Helmholtz Coils. As a result of the fully aligned nature, UCS increased to the point that there was no statistically significant difference between the direction of alignment and the ice growth direction. Prior to that work 80% microstructural alignment was the most microstructural alignment achieved in iron oxide scaffolds magnetically freeze-cast using Helmholtz coils [14, 22]. Achieving the additional 20% to get to effectively 100% microstructural alignment had a significant impact on UCS, as it nearly tripled, from 4 to 11 MPa [14, 22, 23].

Despite how well known, it is that microstructural alignment increases mechanical properties, little is known about why this is the case or how to exploit this observation for design purposes. More specifically, little work has been done to explore the effect alignment has on the failure mode of lamellar walls. In previous freeze-casting work, decreased pore aspect ratio and lamellar wall spacing lead to increased UCS [24–28]. Further theoretical analysis of that work led the authors to conclude that the decreasing the size of these features caused a change in failure mode from ultimate compressive failure to buckling, which increases UCS of the scaffold [24, 27]. Thus, there is reason to believe a change in failure mode could occur

when the microstructure becomes fully aligned and cause the dramatic increase in strength seen [20]. For example, structures that fail via buckling absorb more energy as they are loaded, compared to those that fail via ultimate compressive failure, causing them to fail in a more gradual manner [29, 30]. In contrast, structures that fail via ultimate compressive failure absorb loads with relatively small deformation and eventually fail in an abrupt manner [31–33]. Often, this abrupt failure causes structures that fail via ultimate compressive failure to fail at lower stresses than those than fail via buckling [24, 28, 31–33]. Thus, identifying and understanding the failure modes and mechanisms at work in a structure or material can lead to more optimized designs to improve performance [26].

Finite element methods (FEM) have the potential to provide novel insight into the behaviors of freeze-cast scaffold microstructures to better understand these aspects. To date, analyzing the mechanical behavior of freeze-cast scaffolds with FEM has been greatly limited by two key challenges. The first major challenge is creating a model that accurately replicates the complex microstructure of freeze-cast scaffolds. Second, meshing a model with such complex features would require many elements making it hard to achieve any level of computational efficiency. Due to these issues, FEM analysis of aligned microstructure behaviors up to this point has been done using models created in CAD with highly simplified microstructures [34–36]. Though these models are insightful, the understanding they can provide into the behavior of freeze-cast scaffolds is limited due to differences in materials used and the inability of CAD models to depict the complex microstructure. Creating a model with a microstructure that more closely resembles that of a freeze-cast scaffold would provide a new level of understanding of their behaviors. More specifically, it would provide an avenue for a deeper understanding of the failure mechanisms of structures with aligned and unaligned microstructures, respectively.

Using images collected via microcomputed tomography (microCT) is a nondestructive way to create models of the freeze-cast scaffolds microstructure accurately [37–42]. Such a model can provide novel insights into the behaviors of structures with varying levels of alignment. Specifically, the failure modes at work can be identified and quantified. Herein, these models will be used to locate the amount of alignment needed for the failure modes of a structure to switch from those of an unaligned structure to an aligned structure. Literature has been published on the amount of alignment given field strengths can create in magnetic freeze-casting [21–23, 43, 44]. Combining this knowledge with the amount of alignment required to see this transition in failure mode would give users valuable insight when designing their setups. In doing so, the application of freeze-cast scaffolds could be greatly expanded.



Methods

Experimental Work

Sample Preparation

Iron oxide (Fe₃O₄) slurries were created with the following composition: 10 vol% Fe₃O₄ (with a particle size of 200 nm; ACROS Organics, Pittsburgh, PA, USA), 1 wt% polyvinyl alcohol (Alfa Aesar, Ward Hill, MA, USA) and 1 wt% polyethylene glycol (Alfa Aesar, Ward Hill, MA, USA) as binders, and 1 wt% Darvan 811 (R. T. Vanderbilt Company, Inc., Norwalk, CT, USA) as a dispersant, along with water as a freezing agent Slurries were then sonicated at 42 kHz for 12 min and directionally frozen at a rate of -10 deg/min. Four scaffolds with fully aligned microstructures were created by applying a 20mT oscillating magnetic field generated by Helmholtz Coils during freezing. To create 4 scaffolds with an 80% aligned microstructure, a 7.8 mT field was applied during freezing. An additional four scaffolds were frozen without any magnetic field applied during freezing to create unaligned microstructure. After freezing samples were sublimated at 0.047 mBar and -51 °C for 72 h. The green samples, or samples that have completed the sublimation step, are then sintered in an open-air Keith KSK-12 1700 furnace (Pico Rivera, CA, USA) at 1150 deg C for 35 min at heating and cooling rate of 2 deg/min. The resulting structure of the process is 18 mm in height and 6 mm wide and will be referred to as a scaffold.

Structural Analysis

A one mm slice was removed from each scaffold and imaged using a FEI Quanta 600FE-ESEM (FEI, Hillsboro, Oregon, USA) scanning electron microscope (SEM). Images were collected using an accelerating voltage of 7.0 kV and 100×magnification. From these images, the microstructural alignment was analyzed and quantified using ImageJ via procedures previously established [16, 22]. This procedure was used to quantify scaffolds freeze-cast with the field off and on, respectively, during freezing. The goal of microstructural analysis was to the desired amount of microstructural alignment seen in previous work recreated in this work before proceeding with microCT scans. In total, 4 slices were analyzed for field and field off scaffolds, respectively.

Mechanical Testing

Fifteen sintered scaffolds were cut into roughly 4mm³ volumes for mechanical testing. Ultimate compressive strength and stress for the direction of microstructural alignment was

measured using an Instron 5967 load frame with an Instron 30-kN load cell (Norwood, MA, USA). These data were used to construct stress–strain curves for scaffolds with 100%, 80%, and 25% (referred to in this work as unaligned) microstructural alignment.

Finite Element Analysis Work

Zeiss MicroCT Scan

An X-ray microCT scan was taken of one freeze-cast scaffold subject to the magnetic field during freezing and one fabricated without the magnetic field with an of area 2 mm² and a thickness 1 mm. A voxel size of 0.5 mm and a window size 0.967 mm² were used. The current used was 60 kV and 108 microamps.

Model Based on MicroCT Image Reconstruction

The Synopsys® Simpleware software (Exeter, England) was used to create a 3D model from microCT scanned images [45]. Images were thresholded in the software. Only Fe₃O₄ of the scaffolds and air were subject to segmentation. Thus, given the difference in densities between the two lend themselves to relatively straightforward segmentation via thresholding. Thresholded images were then stacked at 0.5 um spacing to create a 3D model. Island removal and close gap techniques were also used to ensure continuity throughout the model [46]. The model was then cropped to create a representative volume element (RVE) and mesh for use in finite element software Abaqus [47].

Convergence studies were used to define the necessary element mesh size and the volume of the RVE. Quadratic tetrahedral elements (C3D10 in Abaqus) were used in this work. Initially, linear tetrahedral elements were used and resulted in contact issues in the model. Quadratic tetrahedral elements excel at meshing intricate geometries and features and therefore were employed in this work to help alleviate the contact issues seen when linear tetrahedral elements were used [48]. A 0.14 mm \times 0.14 mm \times 0.04 mm model volume was used to converge on mesh element size. To determine a volume that was representative of the scaffolds, computationally efficient convergence studies were used to determine the thickness of the model. A face area of 0.14 mm³ was determined necessary to encapsulate sufficient variability in model alignment to deduce trends. In compression tests, stress was modeled for convergence, while eigenvalues and load proportionality factors were the subject of convergence in buckling analysis. Stress was converged on since it is the metric that will be used to calculate UCS values in this work [49]. Reaction forces were summed over the face of the applied load divided by the nominal area of the face to calculate stress. From the nonlinear buckling



analysis, the buckling eigenvalue and load proportionality factor were the quantities extracted to determine the critical buckling stress. Thus, convergence was also achieved on those quantities to ensure results obtained from the nonlinear model were independent of mesh [49]. Based on the results of the convergence studies a mesh with minimum element size of 0.001 mm and thickness of 0.06 mm were selected. Mesh settings resulted in O(1e6) degrees of freedom.

Failure Mode Determination

To understand the failure modes of the different degrees of alignment, buckling analyses were run. Nonlinear eigenvalue buckling analysis was used to compute the critical buckling stress of each FE model. The critical buckling stress for each model was then compared to the experimental ultimate compressive strength (UCS) for the fully aligned, 80% aligned, and unaligned models. Experimental UCS was defined as the max stress value. For the additional alignment models the critical buckling stress was compared to UCS values extracted from FEA compression tests. Where the critical buckling stress was lower than the UCS, buckling was the mode of failure. Where the UCS was lower than the critical buckling stress, ultimate compressive failure was determined to be the failure mode.

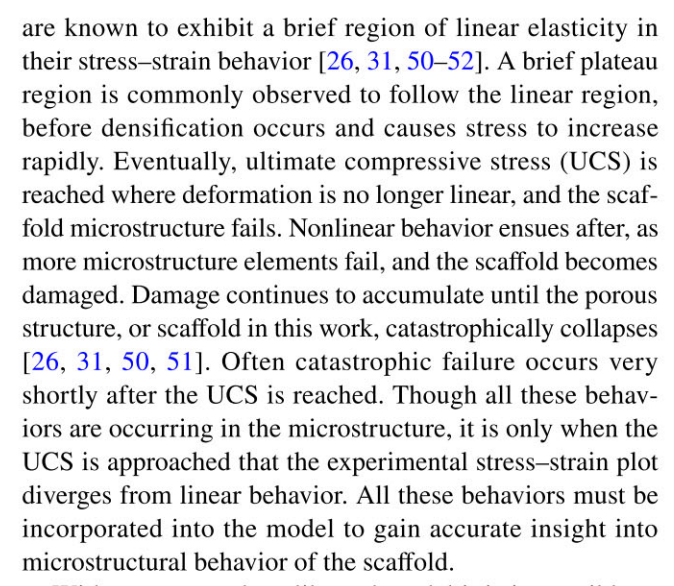
CAD Model Creation and Failure Mode Analysis

CAD models were created to better understand their deficiencies in modeling freeze-cast scaffolds. Models were created with fully aligned, 80% aligned, and unaligned microstructures and modeled using FEA to compare with models created via microCT. CAD models were created with the same dimensions as the microCT models (0.14 mm×0.14 mm×0.06 mm) to ensure CAD models had as accurate behaviors as possible. FEA simulations with boundary conditions replicating compression tests were performed first to obtain UCS data for the CAD models. Nonlinear buckling simulations were run next to calculate the critical buckling stress. Failure mode of the scaffold was determined by comparing the critical buckling stress and UCS as was done above for the microCT models.

Results

Calibration and Validation of FEA Model

Elastic and damage model material properties of the fully aligned model were calibrated to match stress—strain plots collected from compression testing fully aligned structures. To do so, boundary conditions replicating a compression test were used on the FEM model. Porous brittle materials



Without a properly calibrated model it is impossible to gain accurate insight into microstructural behaviors of scaffolds. Therefore, given these regions preceding UCS exhibit relatively linear behavior, linear properties will be used to model them [53]. To calibrate the linear elastic region of the model the Young's modulus and Poisson's ratio are adjusted. After linear behavior has concluded in the scaffold, the scaffold begins to yield. Modeling this requires the use of a damage model. A Johnson-Holmquist damage model is commonly used to model damage in ceramics and other brittle materials and is used to model the nonlinear region in this work [54, 55]. Other damage models, such a phase field damage model, were considered, but the Johnson-Holmquist model was eventually selected for its relative ease of implementation and the lower computational cost compared to other models considered. The parameters of the Johnson-Holmquist model were implemented into the model using the exponential form of the exponential form of the Drucker-Prager model [52, 53]. In the Johnson-Holmquist model, the intact strength of as structure, σ_i^* , is defined as

$$\sigma_i^* = A \left(\frac{P}{P_{\text{HEL}}} + \frac{T}{P_{\text{HEL}}} \right)^N \tag{1}$$

where A and N are material parameters, P is the actual pressure, $P_{\rm HEL}$ is the pressure at the Hugoniot elastic limit (the stress at which a material transitions from elastic to plastic deformation under shock loading), and T is the maximum tensile pressure a material can with stand [54]. The general exponent form of the extended Drucker–Prager model is defined as

$$\sigma = \frac{1}{a^{1/b}} \left(P + P_t \right)^{1/b} \tag{2}$$



where σ is the stress, a and b are material parameters, P_t is the hardening parameter that represents the hydrostatic tension strength of the material, and P is the equivalent pressure stress[56]. Variables from the Johnson–Holmquist model in Eq. 1 can then be substituted into Eq. 2 to get an equation similar to the intact strength of the Johnson–Holmquist model[56]:

$$\sigma_i^* = \frac{A_{\text{HEL}}}{P_{\text{HEI}}^N} (P + T)^N \tag{3}$$

Equation 3 can then be compared with Eq. 2 above to obtain the material parameters a and b that can be calibrated to implement the Johnson–Holmquist model using the exponential form of the Drucker–Prager damage model, where a and b are as follows [56]:

$$a = \frac{P_{\text{HEL}}}{\left(A_{\text{HEL}}\right)^{1/N}} \tag{4}$$

$$b = \frac{1}{N} \tag{5}$$

Minimal literature exists to date on the values of the variables used in the Johnson–Holmquist model. This can be overcome by using the Drucker-Prager model implementation. When the Drucker-Prager implementation of the Johnson-Holmquist model is used one is no longer confined to the variables of the Johnson-Holmquist model [56]. Only two variables require calibrating, which eases calibration significantly. To calibrate the model, linear properties and parameters for the Drucker-Prager model are input and loading is applied to simulate a compression test. From the simulation, stress and strain data are extracted and plotted against experimentally collected compression data. The Drucker-Prager model parameters are then iterated until an R^2 value of 0.8 was achieved between the experimental stress data and stress generated by the model. Final parameters from the calibration process are shown in Table 1. The hardening parameters used in the damage model are shown in Table 2.

An R^2 value of 0.93 (p < 0.01) was achieved when comparing the model data computed using the final parameters to the experimental data (see Fig. 1)[37, 38].

Table 1 The linear elastic parameters and the parameters for the Johnson–Holmquist model implemented using the exponential form of the Drucker–Prager model calibrated to fit the model

Linear elastic		Exponential Drucker-Prager		
E (MPa)	ν	a	b	Dilation angle
980	0.28	0.0001	1.6667	10

Table 2 The hardening parameters used in Drucker–Prager implementation of the Johnson–Holmquist model

Stress (MPa)	Plastic strain	
Hardening parameters		
30	0	
31	0.01	
32	0.02	
33	0.03	
34	0.04	
35	0.05	

Based on this, the model parameters were deemed to be accurately calibrated. Experimentally measured elastic modulus values for freeze-cast scaffolds show large amounts of variability.

Validating finite element models with experimental data is essential to assessing if the simulated output captures the principle mechanisms. Stress—strain data collected from experimental compression tests for unaligned and 80% aligned scaffolds are used in this work to validate the material properties calibrated to fit the fully aligned model. Two scaffolds with each amount of microstructural alignment, 80% and unaligned, were fabricated and compression tested to obtain validation data. Structural analysis was also performed using SEM to confirm scaffolds had the desired amount of microstructural alignment. Microstructural analysis confirmed the desired amount of alignment was achieved. Thus, this work was able to recreate the microstructural alignment achieved in previous work and the magnetic alignment is deemed reproducible [23]. In the linear region of

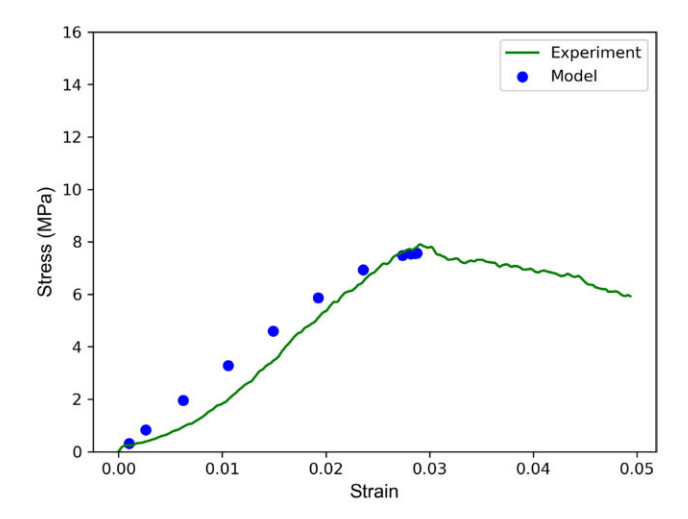


Fig. 1 A stress–strain plot for a fully aligned model generated by the FEA model using the material parameters in Tables 1 and 2 is plotted against experimentally collected compression data. The hardening parameters and linear properties of the model show good agreement with the model with an R^2 value of 0.93



freeze-cast scaffolds, much variability can be seen as a result of the freezing process [20, 22, 23, 43, 44]. Even when uniform freezing rates are attempted small changes in the rate occur [26, 57, 58]. These small changes cause nonuniform pores to form. Even if they occur in small amounts, these nonuniform pores result variability of freeze-cast scaffold behavior in the linear region [6, 27, 57, 58]. UCS behavior is more consistent in freeze-cast scaffolds, and therefore it is more commonly analyzed to understand the behavior of scaffolds and cellular ceramics as a whole [4, 57–59]. Therefore, UCS is more commonly analyzed in freeze-cast scaffolds and will be used to validate material properties used in this work.

The material models and parameters were validated for the 80% aligned and unaligned cases. Loading simulating a compression test was applied to each the 80% aligned and unaligned models using the material properties calibrated for the fully aligned model (properties shown in Table 1). The model was deemed validated if the UCS of the simulated compression test was within the 95% confidence interval of the experimental UCS values. For both the 80% aligned and unaligned models this was the case, as can be seen in Fig. 2 shows the mean of the experimental data (green dots) with the 95% confidence interval (green bars) and the UCS outputted by the model (blue dots) generated using the material properties shown in Tables 1 and 2. The model generated

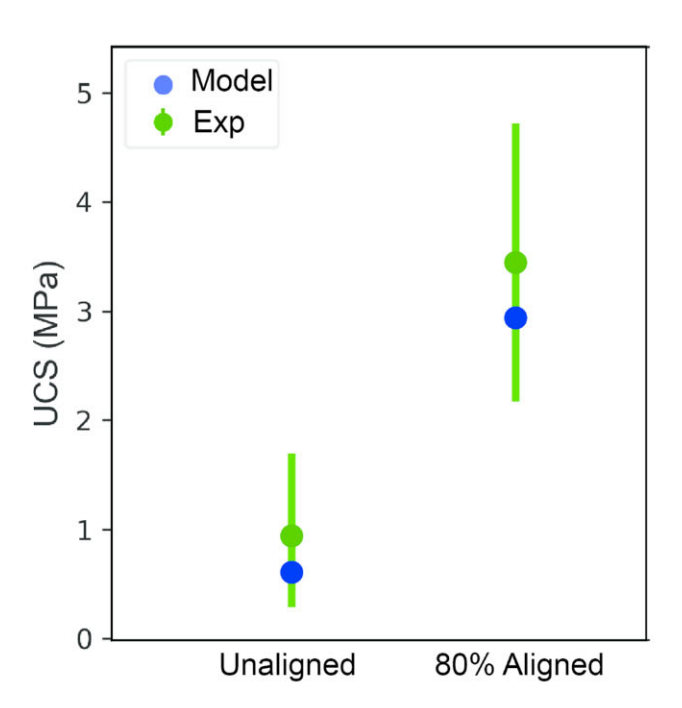


Fig. 2 The mean of the experimental data (green dots) with the 95% confidence interval (green bars) and the UCS outputted by the model (blue dots) generated using the material properties shown in Tables 1 and 2. The model generated data falls within the 95% confidence interval for both the 80% and unaligned data. Thus, the model parameters are validated

data falls within the 95% confidence interval for both the 80% and unaligned data. Thus, the model parameters are validated. This validation enables the microstructure within the model to accumulate damage and then eventually fail in a way that accurately shows what occurs in experimental scaffolds. Additionally, it can provide UCS data for models of additional alignment for which no experimental data exists (e.g. 70%, 90%, and 95% aligned models). It is also of note that since these microCT scans were collected from actual freeze-cast scaffolds, real-world imperfections, such as variability in particle distribution and porosity, that occur in scaffolds are present in the models. The presence of these imperfections further improves the accuracy of the insight gained from these models.

Experimental Stress-Strain Analysis

Based on experimental stress-strain behavior, it is hypothesized that fully aligned structures fail via buckling. In the stress-strain plot for the fully aligned model, stress increases in a linear fashion briefly at the beginning before reaching a peak (see Fig. 3). As is characteristic of porous ceramics, following this peak there is a plateau region where stress remains relatively constant due to pores collapsing [26, 30, 50]. Following the plateau, stress increases rapidly as densification occurs. As stress is approaching a peak, stress begins to exhibit oscillating behavior. This oscillating behavior seen in the stress-strain curve is a result of individual walls within the structure buckling [26, 30, 33, 51, 59]. Eventually after the structure has significantly densified, or enough walls have buckled within the

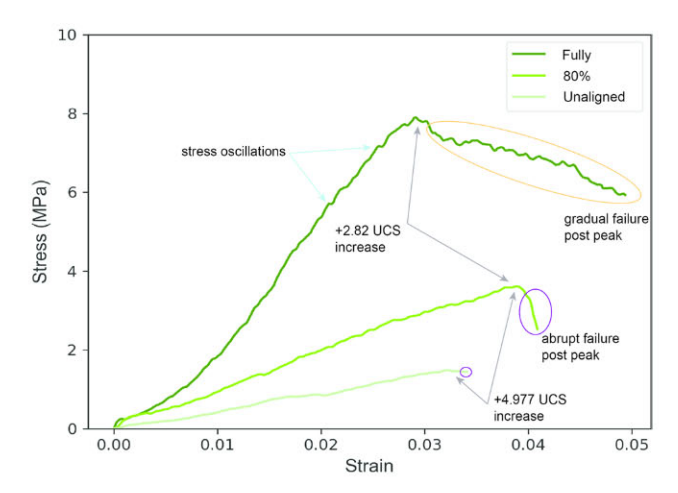


Fig. 3 Experimentally collected stress-strain plots for models with unaligned, 80% aligned, and fully aligned microstructures. The abrupt failure of the unaligned and 80% aligned models is highlighted using purple circles, while the more gradual failure of the fully aligned model is highlighted using an orange circle. Additionally, two instances of the oscillating stress behavior are highlighted by the light blue arrows



structure that the overall ability of the scaffold to support a load is reduced, a peak stress is reached. Characteristics such as oscillating stress behavior leading up to the peak, and the structure continuing to strain post peak are indicative of a structure failing via buckling. Experimental evidence of this occurring in freeze-cast scaffolds has been shown by Sueba et al. [26]. Previous work has shown that the buckling of lamellar walls in cellular solids is an elastic instability and causes progressive failure. A defining trait of ultimate compressive failure in porous scaffolds is stress reaching its peak, the ultimate compressive stress, and then abruptly dropping due the catastrophic failure of the structure [26, 60, 61]. In fully aligned scaffolds, this abrupt drop in stress post peak is absent (again see stress-strain plot in Fig. 3). Additional work has shown that the compressive strength of freeze-cast scaffolds can be increased by improving resistance to buckling within, causing materials to fail at higher strengths [26, 62]. In this work, scaffolds that fail via buckling fail at higher strengths than those that fail via ultimate compressive failure. In unaligned scaffolds, the lack of microstructural alignment causes walls to collapse upon themselves before buckling can occur. Thus, failures stresses in this work are higher under buckling failure modes than when scaffolds fail via ultimate compressive failure. The stress exhibits increasing stress oscillation behavior post peak, indicating additional buckling of scaffold walls. Though some occurs before the peak, the stress oscillation increases and becomes much more obvious after the peak is reached. This behavior coupled with the absence of immediate catastrophic failure post peak leads to the hypothesis that fully aligned scaffolds fails via buckling.

Experimental stress-strain results for unaligned scaffolds suggest they fail via ultimate compressive failure. Characteristics of porous structures are not as clear on the stress-strain plot of unaligned scaffolds as they are on the fully aligned structure (Fig. 3). The linear region occurs at the beginning, followed by the plateau region and then densification. The low stress values and weakness of the unaligned scaffolds make these regions difficult to distinguish from one another. One characteristic that is clearly distinguishable in the stress-strain plot of the unaligned structure is the abrupt failure that occurs as the peak is reached. This abrupt failure indicates failure via ultimate compressive failure [26, 29, 31, 33, 60, 61]. In the stress-strain plot of the unaligned scaffold, there is minimal stress oscillation. In the stress-strain plot of fully aligned scaffolds, lots of stress oscillation occurs, as individual walls buckle. In contrast in the stress-strain curve of the unaligned structure, little stress oscillation behavior is seen. Rather the stress-strain curve is relatively smooth throughout. This combined with the abrupt failure leads to the hypothesis that the unaligned scaffold fails via ultimate compressive failure.

Ultimate compressive failure is also hypothesized to be the failure mode of 80% aligned scaffolds based on experimental stress-strain data. The 80% aligned scaffolds includes behaviors seen in the fully aligned and unaligned scaffolds. Unlike in the unaligned scaffold, the stress-strain plot of the 80% aligned scaffold is not completely smooth. There is some oscillating stress behavior as the stress approaches the UCS (see Fig. 3). Yet, once the UCS is reached, abrupt failure occurs. The combination of these two behaviors makes it less clear which failure mode is occurring. Given how signature of ultimate compressive failure the abrupt catastrophic failure is, it is hypothesized that it is the primary failure mode occurring in the 80% aligned scaffold. Based on the stress-strain plot characteristics of the fully aligned scaffold, it can be further hypothesized that aligned walls fail via buckling and cause the oscillating stress behavior. Given 80% of the walls are aligned, it makes sense that some stress oscillation occurs in the 80% alignment. Yet, given how abruptly the scaffold catastrophically fails, it is hypothesized 80% alignment is not a sufficient enough amount of alignment to cause the scaffold's primary failure mode to shift from ultimate compressive failure to buckling.

FEA Failure Mode Analysis

The hypothesis that the fully aligned model fails via buckling and the unaligned model fails via ultimate compressive failure were confirmed by FEA using the microCT model.

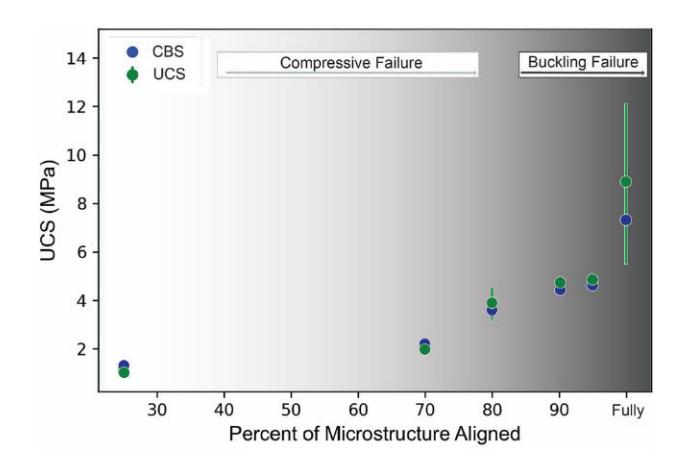
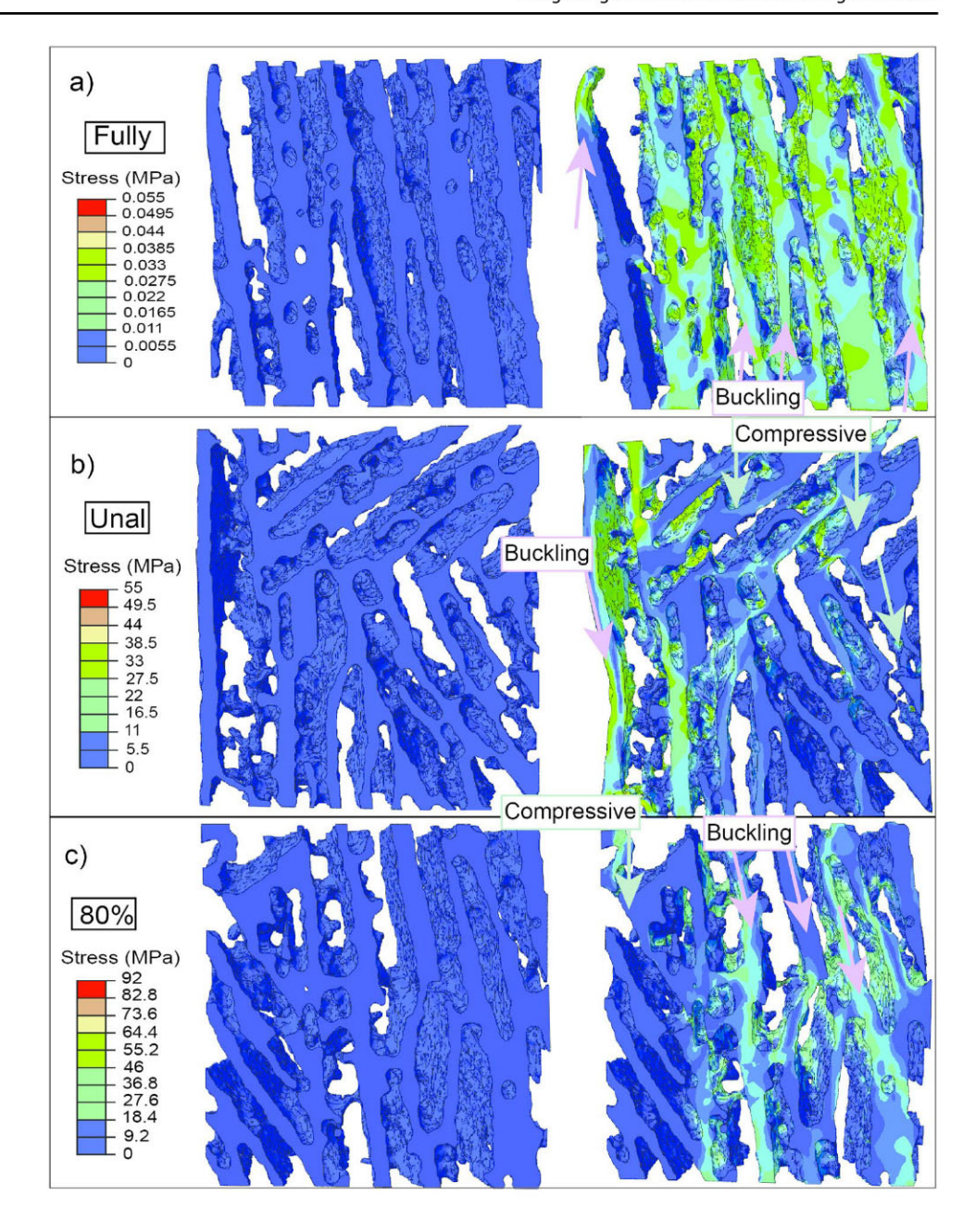


Fig. 4 The UCS and FEM calculated critical buckling stress (CBS) for models with unaligned, 70%, 80%, 90%, 95%, and fully aligned microstructures. The UCS is lower in the unaligned and 70% aligned models, and thus ultimate compressive failure is the mode of failure. At 80% microstructural alignment, this shifts and the critical buckling stress is lower than the UCS for all models with alignments of at least 80%. The transition in failure mode is indicated by the background color in the figure. At 25% alignment, the background is white indicating ultimate compressive failure and as the alignment increases the background darkens to gray indicating the failure mode switching to buckling. The transition in color and thus failure mode can be seen to occur at 80% microstructural alignment



Fig. 5 The stress distribution as the scaffolds are loaded is for a fully aligned model (a), 80% aligned model (b), and an unaligned model (c). Stress maps are shown of the models when they are unloaded (left) and at failure (right). Pink arrows highlight the locations of buckling, while green arrows highlight areas where compressive failure



The critical buckling stress is reached before the yield stress, and therefore, it is determined the fully aligned model fails via buckling. In Fig. 4, the UCS and critical buckling stress are plotted against alignment. Failure mode is indicated by the background color with white representing ultimate compressive failure and gray representing buckling. The way stress is distributed throughout the model further shows the way the aligned microstructure supports loads (see Fig. 5a).

The alignment of the lamellar walls within the fully aligned model distributes the load across the walls, which gives fully aligned freeze-cast scaffolds their strength [52]. In the model, most walls are aligned, but in being aligned they branch and are connected to other walls by cross bridges. All this complexity increases the strength and

extends the lifetime of the scaffold. MicroCT enables the creation of a model that accounts for all these intricacies. Ashby plots are commonly used to show how strength varies with density in cellular materials [4, 33, 51]. In Fig. 6, an Ashby plot can be seen in with the fully aligned, 80% aligned, and unaligned scaffolds plotted alongside the models for cellular materials proposed by Gibson and Ashby [4, 26, 33, 51]. Based on literature, it is expected that models that fail via buckling failure should align with the behavior of the honeycomb model [51]. In Fig. 6, this can be seen to be the case (dark blue star) which further shows that fully aligned models fail via buckling. Eventually, when the fully aligned microstructure can no longer support the load, the outermost wall began to buckle. This can be seen in



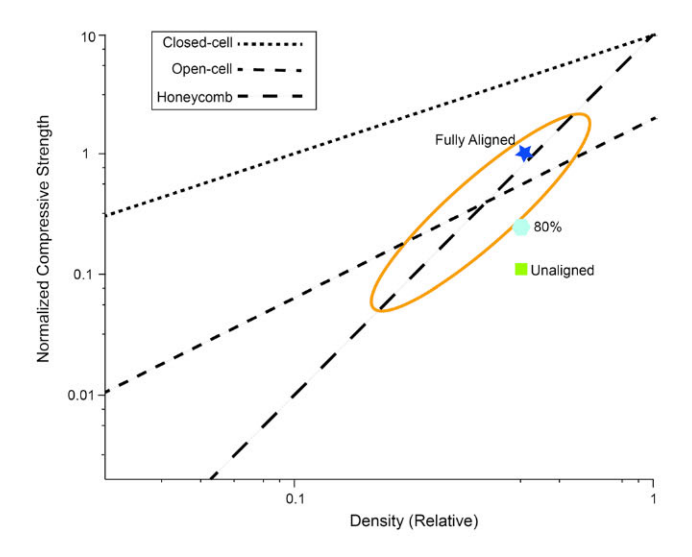


Fig. 6 An Ashby plot with fully aligned (dark blue star), 80% aligned (light blue hexagon), and unaligned (green square) scaffolds plotted along with the honeycomb, open-cell, and closed-cell models proposed by Ashby. The general range of behaviors of freeze-cast scaffolds, which are known to behave like honeycomb structures, are shown by the orange ellipse. The three models created in this work fall within or near the freeze-casting range, with the full aligned model falling on the end with greater relative strength and the unaligned model falling on the end with lower relative strength. Based on Ashby's work, models that fail via buckling should align with the honeycomb model. This can be seen to be the case, thus further showing that full aligned scaffolds fail via buckling

supplementary video 1. On the stress—strain curve, the peak would be reached and the stress would drop since the scaffold can no longer support the load. Thus, the fully aligned model fails via bucking.

The hypothesis formed based on experimental stress-strain data for unaligned scaffolds were confirmed in FEA trials. UCS is lower than critical buckling stress, thus unaligned scaffolds fail via ultimate compressive failure. Visual inspection of the FEA model, specifically of the stress distribution and displacement, throughout the loading process further illustrates these findings (see Fig. 5 b). This failure mode can also be seen in supplementary video 2. In the aligned model, stress is distributed throughout the walls. In contrast to the fully aligned structure, the stress is more concentrated where the different alignment directions come together in the unaligned model. Eventually the stress concentrations cause the microstructure to collapse and the scaffold fails catastrophically. Thus, unaligned scaffolds fail via ultimate compressive failure.

The failure mode of the 80% aligned scaffold was determined to be buckling rather than ultimate compressive failure as was hypothesized based on experimental stress–strain curves. This is shown in supplementary video 3. Based on findings from the fully aligned model, it is known that aligned walls fail via buckling. Combining this knowledge

with the experimental stress—strain plots, the failure of these walls causes oscillating stress behavior. Knowing this, we conclude that the oscillating stress behavior seen in the experimental stress—strain curve of the 80% aligned model leading up to the point of failure resulted from some of the aligned walls within the microstructure buckling.

Enough of the walls failed via buckling that the critical buckling stress was lower than the UCS for the 80% aligned model. Thus, 80% microstructural alignment causes the failure of a scaffold to switch from ultimate compressive failure to buckling. Visually inspecting the FEA results confirms this (Fig. 5c). Stress concentrations formed in the unaligned model caused it to collapse upon itself and fail. The aligned walls support enough of the load that stress concentrations do not form in the unaligned section of the model, thus causing the failure mode to switch. The critical buckling stress is within the 95% confidence interval of UCS values experimentally collected for the 80% aligned model. It is lower than the mean UCS value leading us to conclude the failure mode is buckling. Since the critical buckling stress is within the 95% confidence interval of the UCS data, it can be concluded this failure mode is switching at 80% alignment. These results show that 100% microstructural alignment is not necessary for the failure mode of a scaffold to switch from ultimate compressive failure to buckling and that the switch occurs at 80%.

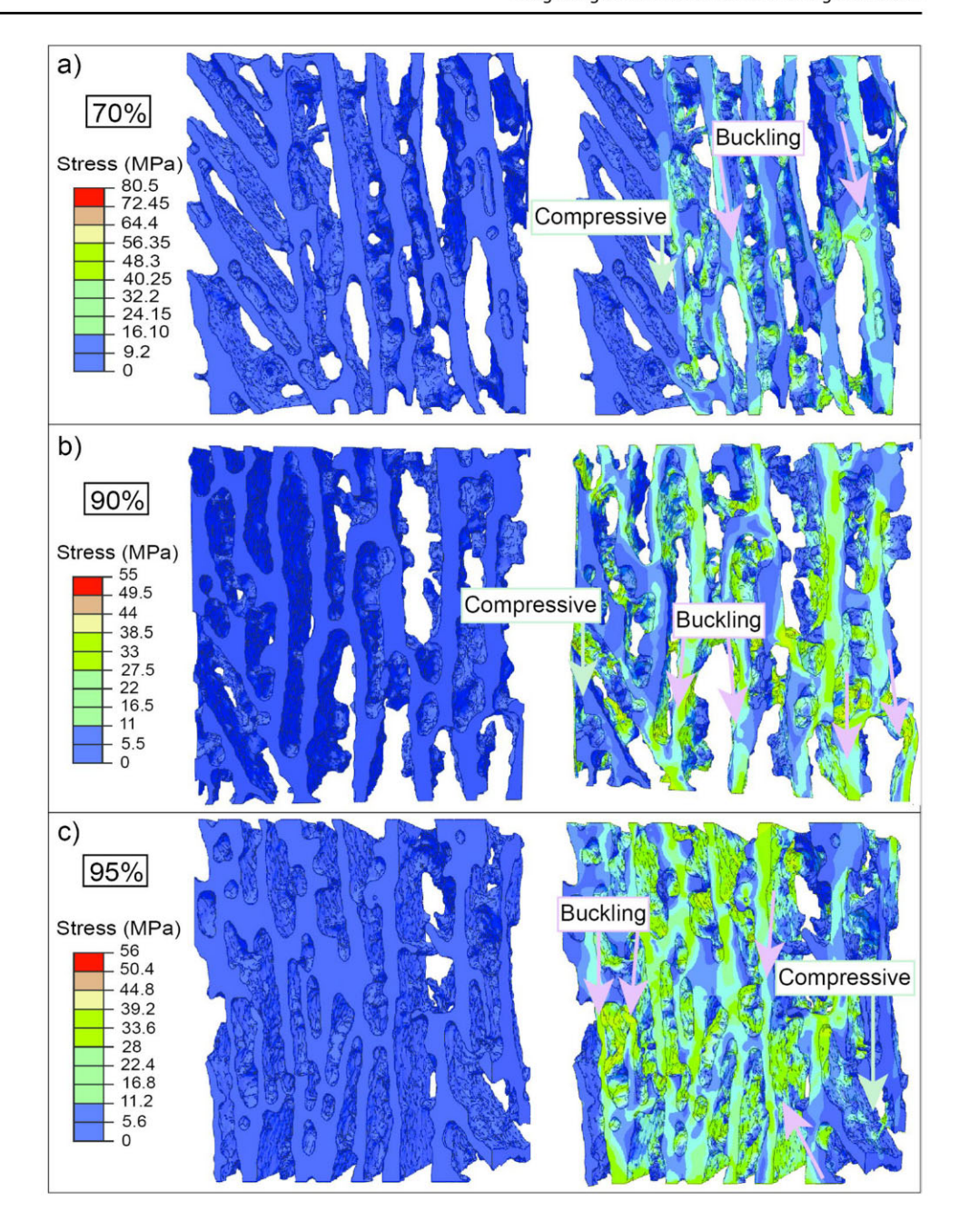
Additional Alignment/Locating Failure Mode Switch

FEM models created from microCT scans in this work provide a unique ability to simulate the effect of microstructural alignment. Such an ability allows for the failure mode switch seen at 80% alignment to be confirmed and provides additional quantitative fields, beyond that of experiment alone. Additional models with 70%, 90%, and 95% microstructural alignment were created (see Fig. 7a, b, and c respectively). Both the 90% and 95% models fail via buckling, while the 70% model fails via ultimate compressive failure (see Fig. 7).

Thus, the change in failure mode of freeze-cast scaffolds occurs between 70 and 80% microstructural alignment. This can be seen in Fig. 4 by background color darkening from white, indicating ultimate compressive failure, to gray, indicating failure by buckling, between and 70% and 80% microstructural alignment. Experimental results show that when microstructural alignment is increased from 80% to effectively 100% that the UCS increases in a statistically significant manner (p < 0.01). The increase in UCS, though it is just a 20% increase in alignment, is over 200% (see Fig. 3). In contrast, when a scaffold goes from being unaligned to 80% aligned (a 55% increase since an unaligned model is deemed to have 25% microstructural alignment), the UCS



Fig. 7 The stress distribution as the scaffolds are loaded is for a 70% model (a), 90% aligned model (b), and a 95% model (c). Stress maps are shown of the models before they are loaded (left) and at failure (right). Pink arrows highlight the locations of buckling, while green arrows highlight areas where compressive failure



increases again by greater than 400%, again with statistically significance (p < 0.01).

This prompts an additional question as to if effectively 100% microstructural alignment is required to see this increase or if the increase occurs in a more linear fashion at increments of alignment between 80 and 100%. Knowing this would prove insightful for applications. If an application requires greater energy absorption but not necessarily the highest strength, microstructures with 80% microstructural alignment could be sufficient, whereas if an application

requires higher energy absorption and wants the highest strength option a fully aligned microstructure could be deemed the suitable choice. Additional models show that the strength does indeed increase significantly when effectively 100% microstructural alignment is achieved. Data generated by the model show that the UCS and critical buckling stress for the 95% aligned model are outside of the 95% confidence interval of the fully aligned model. Thus, the



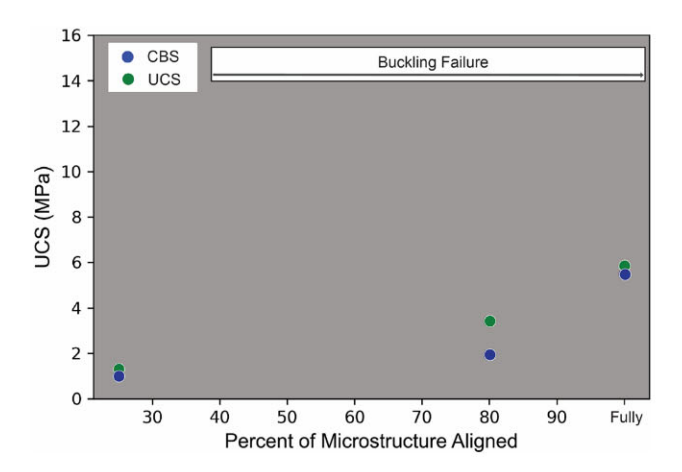


Fig. 8 Critical buckling stress and UCS plotted vs microstructural alignment for CAD models where the green dot is lower, the UCS is lower and the model fails via ultimate compressive failure where the blue dot is lower, the failure mode is buckling. The color shading indicates the failure mode at that point. In the CAD models, the failure mode regardless of alignment remains buckling, as can be seen by the gray shading throughout

increase in strength that comes from getting the remaining 5% of microstructure aligned is substantial.

From the FEA, UCS data were extracted and compared to data from the buckling simulations to determine the failure mode of each model. UCS values for the 90% and 95% models are shown on the plot in Fig. 4. As was done on the previous models, nonlinear buckling simulations were run to determine the critical buckling stress of the 90% and 95% aligned models. In the cases of both the 90% and 95% aligned models, the critical buckling stress was lower than the yield stress and therefore both were determined to fail via buckling. Given these results were from simulation from replicated microstructures, confidence intervals were not generated for them. Despite this, since the microstructural alignment increases the difference between the critical buckling stress and the UCS widens, it can be concluded that the switch occurs at 80%. At 80% alignment, the critical buckling stress is only lower by a quarter of a megapascal. From how close these two values are we can conclude the change in failure mode occurs at 80% microstructural alignment. Though the change in failure mode occurs at 80% microstructural alignment, the greatest increase in critical buckling stress value does not occur until effectively 100% microstructural alignment is achieved. The critical buckling

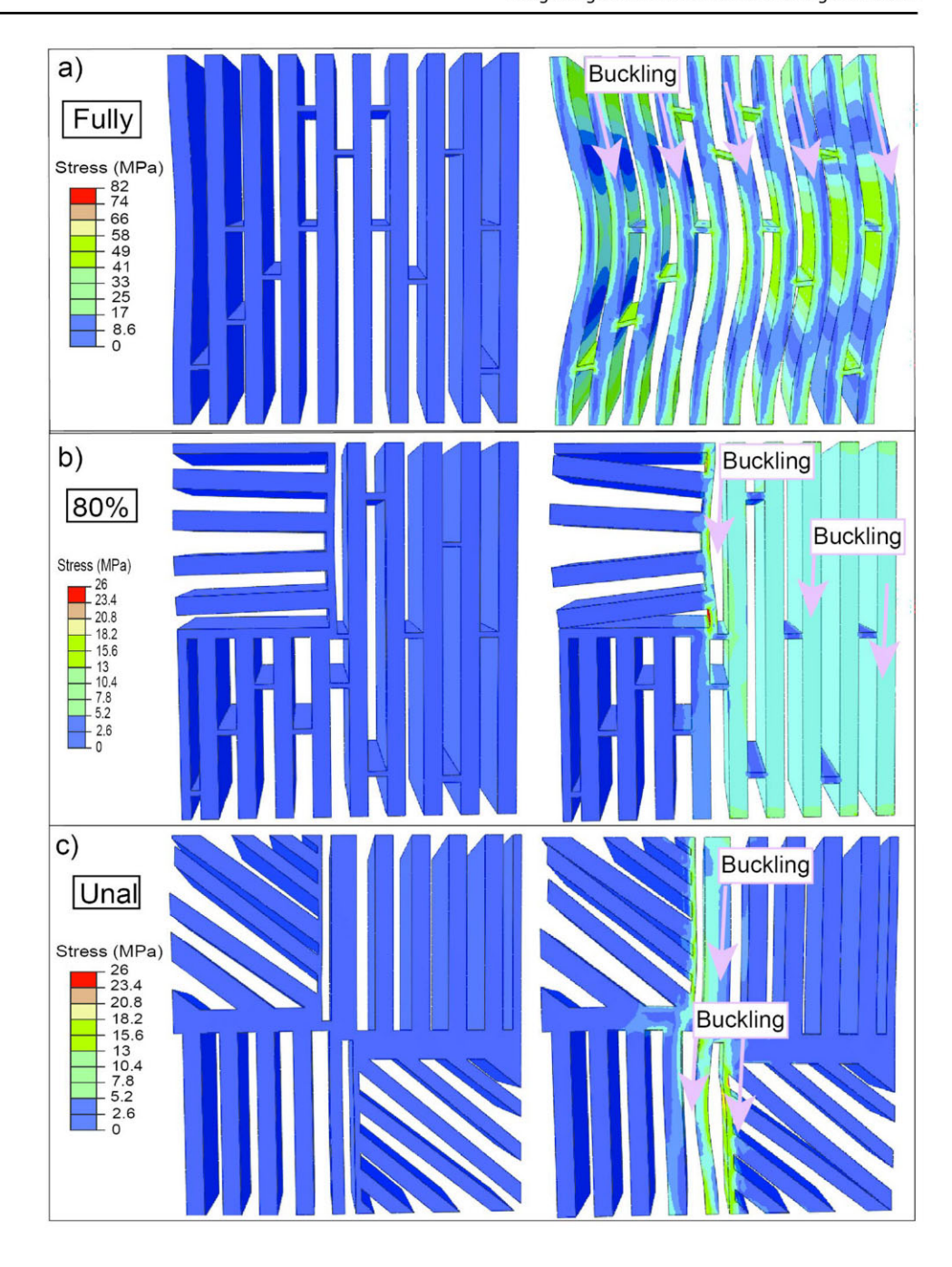
stress of the fully aligned model is higher than that of the 95% aligned scaffold by a statistically significant amount. Thus, to anything short of effectively 100% microstructural alignment will fall short in creating a supremely strong scaffold. Therefore, if applications are looking to manufacture the strongest scaffolds possible, a setup capable of creating a fully aligned microstructure must be constructed. Note only single static loading scenarios were performed in this work. An area for potential future exploration is using microCT models developed in this work to model freeze-cast scaffolds in cyclic loading. Doing so would provide valuable insight into how freeze-cast scaffolds would perform when loaded repeatedly which is important to understand when considering freeze-cast scaffolds for real-world applications.

CAD Model Results

Results from running the same buckling analysis on the CAD (containing simplified microstructures) models highlight the ways CAD models fall short in capturing the behaviors of freeze-cast scaffolds. CAD models are unable to accurately model the failure mode switch. Buckling was the failure model of all models (unaligned, 80% aligned, and fully aligned). The UCS and critical buckling stress are plotted vs microstructural alignments again in Fig. 8. The blue dots corresponding to the critical buckling stress are lower regardless of percent microstructural alignment. The lack of failure mode change is further shown by the uniform blue shading throughout the plot, unlike what is shown in Fig. 4. As the microCT data show, scaffolds with less than 80% microstructural alignment should fail via ultimate compressive failure. The increases in strength seen as microstructural alignment increases in CAD models is much less than in experimental data. With a fully aligned microstructure the UCS is lower than the experimental UCS of an 80% aligned scaffold. These results highlight the importance of microstructural features in affecting the strength and behaviors of freeze-cast scaffolds. The complexities, such as cross bridges and variability in wall thickness, of freeze-cast scaffolds are not captured in CAD models. Their absence causes these shortcomings in results (see Fig. 9). Thus, CAD models of freeze-cast scaffolds are not an accurate tool to gain insight into the microstructural alignment of freeze-cast scaffolds. Models created from microCT scans of scaffolds are able to fully capture all the complexity and intricacies of the



Fig. 9 The stress distribution as the scaffolds created using CAD are loaded for a fully aligned model (a), 80% aligned model (b), and an unaligned model (c). Walls can be seen buckling across the frames from left to right in the all three models. Buckling in the scaffolds is indicated by the pink arrows



microstructure in a highly accurate way that has helped to gain a better understanding of freeze-cast scaffolds.

Conclusions

Using FEM models created using microCT scans provided models a level of intricacy never before achieved in modeling freeze-cast scaffolds. The requisite material model parameters for FEA were calibrated using experimentally

collected compression data. Predicted failure modes were then compared to data from physical experiments for validation of principle mechanisms. The conducted analyses show that the failure mode of scaffolds changes from ultimate compressive failure to buckling when 80% microstructural alignment is achieved. Additional models of 70%, 90%, and 95% were generated to confirm 80% is the location of this switch. These models also showed that scaffold UCS does not increase linearly with alignment from 80 to 100% (see Fig. 10). Rather a large jump in



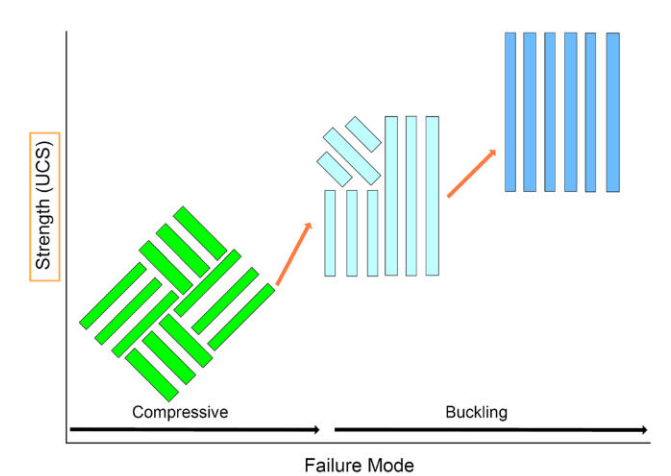


Fig. 10 Representative image showing the change in failure mode that occurs at 80% microstructural alignment. The substantial increases in strength seen when microstructural alignment increases from unaligned to 80%, and 80% to 100% are also highlighted. Note these increases in UCS are not shown to scale

UCS is seen when microstructural alignment is increased from 95% to effectively 100%. Both the knowledge of UCS and failure mode provide important information going forward for created freeze-cast scaffolds better suited for their applications.

Supplementary Information The online version contains supplementary material available at https://doi.org/10.1007/s40192-025-00397-3.

Funding Army Research Office, W911NF-21-1-0062, Steven E. Naleway.

Declarations

Conflict of interest The authors declare that they have no known competing financial interests or personal relationships that could have appeared to influence the work reported in this paper.

References

- Bai H, Walsh F, Gludovatz B, Delattre B, Huang C, Chen Y, Tomsia AP, Ritchie RO (2016) Bioinspired hydroxyapatite/poly(methyl methacrylate) composite with a nacre-mimetic architecture by a bidirectional freezing method. Adv Mater 28(1):50–56. https://doi.org/10.1002/adma.201504313
- Yoshikawa H, Myoui A (2005) Bone tissue engineering with porous hydroxyapatite ceramics. J Artif Organs 8:131–136. https://doi.org/10.1007/s10047-005-0292-1
- Deville S (2010) Freeze-casting of porous biomaterials: structure properties and opportunities. Materials 3:1913–1927. https://doi. org/10.3390/ma3031913
- Deville S (2008) Freeze-casting of porous ceramics: a review of current achievements and issues. Adv Eng Mater 10:155–169. https://doi.org/10.1002/adem.200700270
- Launey ME, Munch E, Alsem DH, Saiz E, Tomsia AP, Ritchie RO (2009) A novel biomimetic approach to the design of

- high-performance ceramic–metal composites. J R Soc Interface 7:741–753. https://doi.org/10.1098/rsif.2009.0331
- Deville S, Saiz E, Tomsia AP (2007) Ice-templated porous alumina structures. Acta Mater 55:1965–1974. https://doi.org/10.1016/j.actamat.2006.11.003
- Frank MB, Naleway SE, Haroush T, Liu C-H, Siu SH, Ng J, Torres I, Ismail A, Karandikar K, Porter MM, Graeve OA, McKittrick J (2017) Stiff, porous scaffolds from magnetized alumina particles aligned by magnetic freeze casting. Mater Sci Eng C 77:484

 492. https://doi.org/10.1016/j.msec.2017.03.246
- Nelson I, Naleway SE (2019) Intrinsic and extrinsic control of freeze casting. J Market Res 8:2372–2385. https://doi.org/10. 1016/j.jmrt.2018.11.011
- Suzuki TS, Sakka Y (2002) Fabrication of textured titania by slip casting in a high magnetic field followed by heating. Jpn J Appl Phys 41(Part 2, No. 11A):L1272–L1274. https://doi.org/10.1143/ JJAP.41.L1272
- Sakka Y, Suzuki TS (2005) Textured development of feeble magnetic ceramics by colloidal processing under high magnetic field.
 J Ceram Soc Jpn 113:26–36. https://doi.org/10.2109/jcersj.113.26
- Mroz M, Rosenberg JL, Acevedo C, Kruzic JJ, Raeymaekers B, Naleway SE (2020) Ultrasound freeze-casting of a biomimetic layered microstructure in epoxy-ceramic composite materials to increase strength and hardness. Materialia 12:100754. https://doi. org/10.1016/j.mtla.2020.100754
- Deville S, Maire E, Lasalle A, Bogner A, Gauthier C, Leloup J, Guizard C (2009) In situ x-ray radiography and tomography observations of the solidification of aqueous alumina particles suspensions part II: steady state. J Am Ceram Soc 92:2497–2503. https://doi.org/10.1111/j.1551-2916.2009.03264.x
- Deville S, Maire E, Lasalle A, Bogner A, Gauthier C, Leloup J, Guizard C (2009) In situ X-ray radiography and tomography observations of the solidification of aqueous alumina particle suspensions—part I: initial instants. J Am Ceram Soc 92(11):2489–2496
- Nelson I, Gardner L, Carlson K, Naleway SE (2019) Freeze casting of iron oxide subject to a tri-axial nested Helmholtz-coils driven uniform magnetic field for tailored porous scaffolds. Acta Mater 173:106–116. https://doi.org/10.1016/j.actamat.2019.05.003
- Porter MM, Yeh M, Strawson J, Goehring T, Lujan S, Siripasopsotorn P, Meyers MA, McKittrick J (2012) Magnetic freeze casting inspired by nature. Mater Sci Eng A 556:741–750. https://doi.org/10.1016/j.msea.2012.07.058
- Frank MB, Hei Siu S, Karandikar K, Liu C-H, Naleway SE, Porter MM, Graeve OA, McKittrick J (2017) Synergistic structures from magnetic freeze casting with surface magnetized alumina particles and platelets. J Mech Behav Biomed Mater 76:153–163. https://doi.org/10.1016/j.jmbbm.2017.06.002
- Biomimetic materials by freeze casting | SpringerLink (n.d.). https://doi.org/10.1007/s11837-013-0606-3. Accessed 20 Feb 2023
- Jang S-M, Park H-I, Choi J-Y, Ko K-J, Lee S-H (2011) Magnet pole shape design of permanent magnet machine for minimization of torque ripple based on electromagnetic field theory. IEEE Trans Magn 47:3586–3589. https://doi.org/10.1109/ TMAG.2011.2151846
- Zijlstra H (1982) Chapter 2 permanent magnets; theory. In: handbook of ferromagnetic materials, Elsevier, pp. 37–105. https://doi.org/10.1016/S1574-9304(05)80088-4
- Schmitz MA, Nelson I, Naleway SE (2023) Control over the mechanical properties of surface-magnetized alumina magnetically freeze-cast scaffolds. J Mater Sci. https://doi.org/10.1007/ s10853-023-09108-9
- Fernquist JR, Fu HC, Naleway SE (2022) Improved structural and mechanical performance of iron oxide scaffolds freeze cast



- under oscillating magnetic fields. Ceram Int 48:15034–15042. https://doi.org/10.1016/j.ceramint.2022.02.032
- Nelson I, Ogden TA, Khateeb SA, Graser J, Sparks TD, Abbott JJ, Naleway SE (2019) Freeze-casting of surface-magnetized iron(II,III) oxide particles in a uniform static magnetic field generated by a Helmholtz coil. Adv Eng Mater. https://doi.org/10.1002/adem.201801092
- Fernquist JR, Naleway SE (2024) Complete control and strengthening over iron oxide porous structures freeze cast under oscillating magnetic fields. J Am Ceram Soc 107:2738– 2749. https://doi.org/10.1111/jace.19591
- Porter MM, Imperio R, Wen M, Meyers MA, McKittrick J (2014) Bioinspired scaffolds with varying pore architectures and mechanical properties. Adv Funct Mater 24:1978–1987. https://doi.org/10.1002/adfm.201302958
- Deville S, Meille S, Seuba J (2015) A meta-analysis of the mechanical properties of ice-templated ceramics and metals. Sci Technol Adv Mater 16:043501. https://doi.org/10.1088/ 1468-6996/16/4/043501
- Seuba J, Deville S, Guizard C, Stevenson AJ (2016) Mechanical properties and failure behavior of unidirectional porous ceramics. Sci Rep 6:24326. https://doi.org/10.1038/srep24326
- Hunger PM, Donius AE, Wegst UGK (2013) Structure–property-processing correlations in freeze-cast composite scaffolds. Acta Biomater 9:6338–6348. https://doi.org/10.1016/j.actbio.2013.01.012
- Aljadani MH (2024) The porosity effect on the buckling analysis
 of functionally graded plates under thermal environment using
 a Quasi-3D theory. Sci Rep 14:30216. https://doi.org/10.1038/s41598-024-79894-y
- Alkhader M, Vural M (2008) Mechanical response of cellular solids: role of cellular topology and microstructural irregularity. Int J Eng Sci 46:1035–1051. https://doi.org/10.1016/j.ijengsci.2008. 03.012
- Murray CM, Mao M, Park J, Howard J, Wereley NM (2023) Visco-elastic honeycomb structures with increased energy absorption and shape recovery performance using buckling initiators. Polymers 15:3350. https://doi.org/10.3390/polym15163350
- Gibson LJ (2003) Cellular solids. MRS Bull 28:270–274. https://doi.org/10.1557/mrs2003.79
- 32. Ashby MF (2005) The properties of foams and lattices. Philos Trans R Soc A Math Phys Eng Sci 364(1838):15–30. https://doi.org/10.1098/rsta.2005.1678
- Gibson LJ (1989) Modelling the mechanical behavior of cellular materials. Mater Sci Eng A 110:1–36. https://doi.org/10.1016/ 0921-5093(89)90154-8
- Yang Z, Niksiar P, Meng Z (2022) Identifying structure-property relationships of micro-architectured porous scaffolds through 3D printing and finite element analysis. Comput Mater Sci 202:110987. https://doi.org/10.1016/j.commatsci.2021.110987
- Gryko A, Prochor P, Sajewicz E (2022) Finite element analysis
 of the influence of porosity and pore geometry on mechanical
 properties of orthopaedic scaffolds. J Mech Behav Biomed Mater
 132:105275. https://doi.org/10.1016/j.jmbbm.2022.105275
- Niksiar P, Meng Z, Porter MM (2021) Multidimensional mechanics of three-dimensional printed and micro-architectured scaffolds. J Appl Mech. https://doi.org/10.1115/1.4051182
- Bourne BC, van der Meulen MCH (2004) Finite element models predict cancellous apparent modulus when tissue modulus is scaled from specimen CT-attenuation. J Biomech 37:613–621. https://doi.org/10.1016/j.jbiomech.2003.10.002
- Gupta S, van der Helm FCT, Sterk JC, van Keulen F, Kaptein BL (2004) Development and experimental validation of a threedimensional finite element model of the human scapula. Proc Inst Mech Eng H 218:127–142. https://doi.org/10.1243/0954411043 22984022

- Shefelbine SJ, Simon U, Claes L, Gold A, Gabet Y, Bab I, Müller R, Augat P (2005) Prediction of fracture callus mechanical properties using micro-CT images and voxel-based finite element analysis. Bone 36:480–488. https://doi.org/10.1016/j.bone.2004. 11.007
- Aziz AA, Saury C, Xuan VB, Young P (2006) On the material characterization of a composite using micro CT image based finite element modeling. In: nondestructive evaluation and health monitoring of aerospace materials, composites, and civil infrastructure V, SPIE, pp. 32–39. https://doi.org/10.1117/12.667766
- Basista M, Węglewski W, Bochenek K, Poniżnik Z, Nowak Z (2017) Micro-CT Finite element analysis of thermal residual stresses and fracture in metal-ceramic composites. Adv Eng Mater 19:1600725. https://doi.org/10.1002/adem.201600725
- Wang L, Jiang K, Yang D (2022) Compression behavior of metal foams with real pore structures through CT scan images. J Iron Steel Res Int 29:1886–1897. https://doi.org/10.1007/ s42243-022-00820-5
- Fernquist JR, Nelson I, Pourkand A, Abbott JJ, Naleway SE (2023) Improved strength and control over surface-magnetized titania porous structures freeze cast under oscillating magnetic fields. Materialia 32:101905. https://doi.org/10.1016/j.mtla.2023.101905
- Nelson I, Varga J, Wadsworth P, Mroz M, Kruzic JJ, Kingstedt OT, Naleway SE (2020) Helical and bouligand porous scaffolds fabricated by dynamic low strength magnetic field freeze casting. JOM 72:1498–1508. https://doi.org/10.1007/s11837-019-04002-9
- 3D image processing solutions—simpleware | Synopsys, (n.d.). https://www.synopsys.com/simpleware.html. Accessed 3 Feb 2025
- Simpleware Datasheet (2022) https://www.synopsys.com/conte nt/dam/synopsys/simpleware/pdfs/simpleware-scanip-datasheet-1222.pdf
- Abaqus, Dassault Systèmes (2023) https://www.3ds.com/products/simulia/abaqus. Accessed 3 Feb 2025
- Maas SA, Ellis BJ, Rawlins DS, Weiss JA (2016) Finite element simulation of articular contact mechanics with quadratic tetrahedral elements. J Biomech 49:659–667. https://doi.org/10.1016/j. jbiomech.2016.01.024
- Zienkiewicz OC, Taylor RL (eds) The finite element method, 5th edn. Volume 2: solid mechanics. http://ndl.ethernet.edu.et/bitst ream/123456789/87890/5/Finite%20Element%20Method%20-% 20Solid%20Mechanics%20-%20Zienkiewicz%20and%20Taylor. pdf
- Rege A (2021) Constitutive modeling of the densification behavior in open-porous cellular solids. Materials 14:2731. https://doi.org/ 10.3390/ma14112731
- Ashby MF, Medalist RFM (1983) The mechanical properties of cellular solids. Metall Trans A 14:1755–1769. https://doi.org/10. 1007/BF02645546
- Ojuva A, Järveläinen M, Bauer M, Keskinen L, Valkonen M, Akhtar F, Levänen E, Bergström L (2015) Mechanical performance and CO₂ uptake of ion-exchanged zeolite A structured by freeze-casting. J Eur Ceram Soc 35:2607–2618. https://doi.org/ 10.1016/j.jeurceramsoc.2015.03.001
- Divakar P, Yin K, Wegst UGK (2019) Anisotropic freeze-cast collagen scaffolds for tissue regeneration: how processing conditions affect structure and properties in the dry and fully hydrated states. J Mech Behav Biomed Mater 90:350–364. https://doi.org/ 10.1016/j.jmbbm.2018.09.012
- Johnson GR, Holmquist TJ (1994) An improved computational constitutive model for brittle materials. AIP Conf Proc 309:981– 984. https://doi.org/10.1063/1.46199
- Holmquist TJ, Johnson GR (2011) A computational constitutive model for glass subjected to large strains, high strain rates and high pressures. J Appl Mech. https://doi.org/10.1115/1.4004326



- Abaqus example problems guide (2016) https://ceae-server.color ado.edu/v2016/books/exa/default.htm?startat=ch02s01aex79. html. Accessed Jan 2025
- Peppin SSL, Grae Worster M, Wettlaufer JS (2006) Morphological instability in freezing colloidal suspensions. Proc R Soc A Math Phys Eng Sci 463(2079):723–733. https://doi.org/10.1098/rspa. 2006.1790
- Soon Y-M, Shin K-H, Koh Y-H, Lee J-H, Kim H-E (2009) Compressive strength and processing of camphene-based freeze cast calcium phosphate scaffolds with aligned pores. Mater Lett 63:1548–1550. https://doi.org/10.1016/j.matlet.2009.04.013
- Seuba J, Deville S, Guizard C, Stevenson AJ (2016) The effect of wall thickness distribution on mechanical reliability and strength in unidirectional porous ceramics. Sci Technol Adv Mater 17:128–135. https://doi.org/10.1080/14686996.2016.1140309
- Adam V, Bergfeld B, Weißgraeber P, van Herwijnen A, Rosendahl PL (2024) Fracture toughness of mixed-mode anticracks in highly porous materials. Nat Commun 15:7379. https://doi.org/10.1038/ s41467-024-51491-7

- Tserpes KI, Labeas G, Pantelakis S (2010) Multi-scale modeling of the mechanical response of plain weave composites and cellular solids. Theoret Appl Fract Mech 54:172–179. https://doi.org/10. 1016/j.tafmec.2010.10.013
- Banda M, Ghosh D (2018) Effects of porosity and strain rate on the uniaxial compressive response of ice-templated sintered macroporous alumina. Acta Mater 149:179–192. https://doi.org/ 10.1016/j.actamat.2018.02.027

Publisher's Note Springer Nature remains neutral with regard to jurisdictional claims in published maps and institutional affiliations.

Springer Nature or its licensor (e.g. a society or other partner) holds exclusive rights to this article under a publishing agreement with the author(s) or other rightsholder(s); author self-archiving of the accepted manuscript version of this article is solely governed by the terms of such publishing agreement and applicable law.

